



Universiteit  
Leiden  
The Netherlands

## Steps towards Inelastic Electron Tunneling Spectroscopy in a dipstick Scanning Tunneling Microscope

Baalbergen, Frederik Bert

### Citation

Baalbergen, F. B. (2022). *Steps towards Inelastic Electron Tunneling Spectroscopy in a dipstick Scanning Tunneling Microscope*.

Version: Not Applicable (or Unknown)

License: [License to inclusion and publication of a Bachelor or Master thesis in the Leiden University Student Repository](#)

Downloaded from: <https://hdl.handle.net/1887/3455581>

**Note:** To cite this publication please use the final published version (if applicable).



---

# Steps towards Inelastic Electron Tunneling Spectroscopy in a dipstick Scanning Tunneling Microscope

---

THESIS

submitted in partial fulfillment of the  
requirements for the degree of

MASTER OF SCIENCE

in

PHYSICS

Author :	F.B. Baalbergen
Student ID :	s1994336
Supervisor :	Prof.dr. Jan van Ruitenbeek
Second corrector :	Prof.dr. Tjerk Oosterkamp

Leiden, The Netherlands, August 2, 2022

# Steps towards Inelastic Electron Tunneling Spectroscopy in a dipstick Scanning Tunneling Microscope

**F.B. Baalbergen**

Huygens-Kamerlingh Onnes Laboratory, Leiden University  
P.O. Box 9500, 2300 RA Leiden, The Netherlands

August 2, 2022

## **Abstract**

Inelastic electron tunneling spectroscopy (IETS) is a tool used to research the vibrational modes in a tunneling junction. This report describes the setup of a cryogenic scanning tunneling microscope (STM). Potentially this STM can be used in the research to the edge modes of graphene edge junctions. Gold samples were used for the calibration of the  $z$  stage of the setup by using two different methods (histogram based/line cut based). Experiments at cryogenic temperatures seemed to have difficulties measuring topographic images at 77 K. These difficulties are most likely caused by condensation of atmospheric gasses still present in the system. To solve this problem, a heater is required to prevent material condensing on the sample or tip. In order to implement IETS in the system it is proposed to use a combination of a heater and thermometer in order to keep the system clean.

# Contents

<b>1</b>	<b>Introduction</b>	<b>1</b>
<b>2</b>	<b>Theory</b>	<b>3</b>
2.1	Elastic transport between electrodes	3
2.2	Transmission probability in tunneling	4
2.3	Simmons model	6
2.4	Inelastic electron tunneling spectroscopy	6
<b>3</b>	<b>Methods</b>	<b>8</b>
3.1	Scanning Tunneling Microscopy	8
3.1.1	Experimental setup	8
3.1.2	Data analysis of STM images	10
3.1.3	Fast axis misalignment correction	10
3.1.4	Piezo hysteresis correction	11
3.1.5	Plane correction	14
3.2	Vacuum and cryogenic system	15
<b>4</b>	<b>Results</b>	<b>17</b>
4.1	Gold on mica samples at room temperature	17
4.1.1	Typical images	17
4.1.2	Piezo hysteresis correction	18
4.1.3	z stage calibration	18
4.1.4	IZ curves	21
4.2	HOPG samples at room temperature	22
4.2.1	Height of flakes	23
4.3	Gold on mica samples at liquid nitrogen temperature	25
4.3.1	Problems during cooldown	25
4.3.2	z stage calibration	28
4.3.3	IZ curves	29
4.4	HOPG samples at liquid nitrogen temperature	30

---

<b>5</b>	<b>Discussion and Outlook</b>	<b>32</b>
5.1	Calibration and measured samples	32
5.1.1	Correction for piezo hysteresis	33
5.1.2	IZ curves	33
5.2	Improvements to improve cryogenic performance	33
5.3	Inelastic Electron Tunneling Spectroscopy	34
<b>6</b>	<b>Conclusion</b>	<b>36</b>
<b>A</b>	<b>Data for other data sets for Au on Mica at room temperature</b>	<b>42</b>
A.1	Data 30 May 2022	43
A.2	Data 28 June 2022	44
A.3	Data 29 June 2022	45
A.4	Data 12 July 2022	46

## Introduction

Graphene is a versatile material that can be used in order to make electrodes. This is previously demonstrated in twisted graphene edge junctions[1]. The junction presented in this paper has possible applications in identifying organic molecules and sequencing genetic material. Besides these applications, this junction also has application to study the chemistry of the graphene edge itself.

The building blocks of graphene are carbon atoms in a hexagonal lattice. At the edge of this pattern the chemical structure is different compared to the bulk 2D material. Besides this, the chemical structure of the edge of the graphene can be altered by edge functionalization[2].

In order to probe the structure of this functionalized edge, many experimental methods can be used. One of these methods is inelastic electron tunneling spectroscopy (IETS). This method can be used to identify the vibrational modes present in the junction. Using these modes, chemical structures can be identified[3, 4]. This technique can be implemented in scanning tunneling microscope (STM) systems to locally probe the vibrational modes[5].

The graphene edge junctions previously studied in the Van Ruitenbeek group used an adjusted STM to control the junction. Therefore it is possible to use this system to study the (functionalized) edge of graphene using IETS. In order to obtain the energy resolution needed to resolve the modes, these experiments need to be performed at cryogenic temperatures.

In this thesis we describe the set up of a cryogenic STM in a dip stick. This microscope is set up and experiments were performed in order to calibrate the system. The main goal was implementing IETS in this system in order

to apply this to graphene edge junctions. Unfortunately it was not possible to do this due to time constraints.

In chapter 2 the theory of quantum tunneling and IETS is discussed. After this, the experimental methods and the data processing is discussed in chapter 3. The results obtained using these methods are shown in chapter 4. Finally the results and recommendations for follow up research are discussed in chapter 5.

# Chapter 2

## Theory

The scanning tunneling microscope (STM) is a technique in the scanning probe microscopy family. By moving a tip over the surface of a sample, the topography of this sample is measured. Besides this, using scanning tunneling spectroscopy (STS), also material properties like the local density of states can be measured[6]. In a STM a bias is applied to the junction and the tunneling current is monitored to obtain a fixed distance between the tip and sample. The tip does not touch the sample, therefore classically there would be no current flowing through the junction. In quantum mechanics, particles such as electrons have a chance to tunnel through an area with a larger potential energy than the energy of the particle. This is caused by the wave function penetrating the classically forbidden region for the particle. The amplitude of the wave function decreases exponentially the further you enter the forbidden region. If two conducting materials are close enough, the chance for an electron to jump through the forbidden region, becomes so large that a current is measurable. This phenomenon is called quantum tunneling. In this chapter a model for describing quantum tunneling is discussed.

### 2.1 Elastic transport between electrodes

In this study, we will look at tunneling junctions in an STM. By applying a bias to this junction, a current will flow through the junction. This current is caused by electrons tunneling through a potential barrier.

Our junctions can be modeled as two electron reservoirs with a well defined electron density of states (DOS) and occupation probability. Between these two reservoirs, is a junction with a transmission probability  $T(E) =$



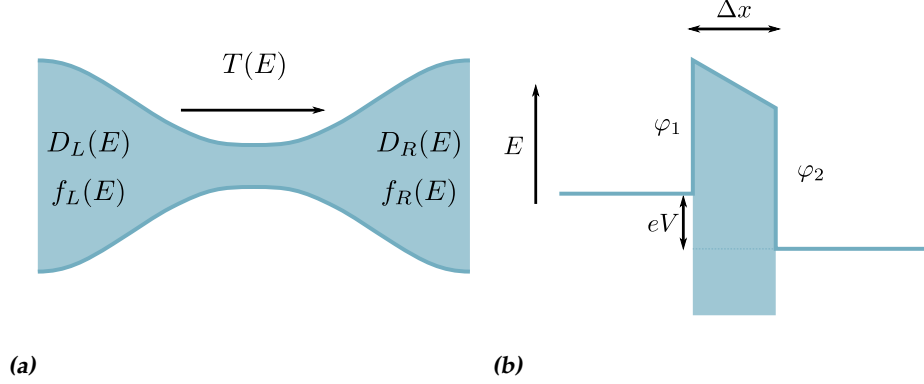


**Figure 2.1:** (a) Schematic situation showing the junction. On the left(right) we have an electron reservoir with a DOS,  $D(E) = \frac{dk}{dE}$  and occupation function  $f_L(E)$  ( $f_R(E)$ ). Between these reservoirs, we have a junction indicated by a restriction with a transmission function  $T(E)$ . (b) Model for the potential  $V(x)$  in the tunnel junction.  $\varphi_1$  ( $\varphi_2$ ) is the workfunction of the sample (tip).  $eV$  is the potential applied between tip and sample and  $\Delta x$  is the distance between tip and sample.

$|t(E)|^2$  that is a function of electron energy. A schematic view of this junction can be found in figure 2.1a. The current flowing through this junction can be described as

$$I(V) = \frac{2e}{h} \int T(E) [f_L(E) - f_R(E)] dE.$$

In this model, only electrons close to the Fermi surface take part in conduction. Only electrons in a state unoccupied in the other electrode can take part of elastic tunneling through the junction due to the Pauli exclusion principle. This is shown in the model by the term  $f_L(E) - f_R(E)$  [7, 8, 9].

## 2.2 Transmission probability in tunneling

In electronic tunneling junctions, there is no physical contact between the two electrodes. The complete current going through the junction is caused by the quantum mechanical tunneling effect. In this effect, it is important to take the wave function of the electrons into account. For the first part of the derivation of this transmission probability, we will follow the derivation called the Wentzel-Kramers-Brillouin (WKB) approximation as described in Sakurai [10]. Using the WKB approximation in STM is previously also described in multiple papers [11, 12]. The wave function of electrons can be described by the Schrödinger equation in 1D

$$\frac{d^2 u_E(x)}{dx^2} + \frac{2m}{\hbar^2} (E - V(x)) u_E(x) = 0, \quad (2.1)$$

where  $u_E(x)$  is the 1D waveform,  $m$  is the mass of the electron,  $\hbar$  is the Planck constant,  $E$  is the energy of the electron and  $V(x)$  is the potential of the tunnel junction. By defining  $k(x) = \sqrt{\frac{2m}{\hbar^2} (E - V(x))}$  we can write the Schrödinger equation as

$$\frac{d^2 u_E(x)}{dx^2} + (k(x))^2 u_E(x) = 0. \quad (2.2)$$

By taking an Ansatz, the wave function in a material can be written as

$$u_E(x) \approx \exp\left(\frac{i}{\hbar} W(x)\right).$$

This now gives the differential equation

$$i\hbar \frac{d^2 W(x)}{dx^2} - \left(\frac{dW(x)}{dx}\right)^2 + \hbar^2 k(x)^2 = 0. \quad (2.3)$$

Now we assume that  $\hbar \left| \frac{d^2 W(x)}{dx^2} \right| \ll \left| \frac{dW(x)}{dx} \right|^2$  to obtain

$$W(x) \approx W_0(x) = \pm \hbar \int^x d\xi k(\xi).$$

Now we can approximate the wave function  $u_E(x)$  using the potential. The used potential of the junction is shown in figure 2.1b. This potential can be approximated in the barrier with width  $\Delta x$  by  $V(x) \approx \bar{\varphi} = \frac{\varphi_1 + \varphi_2}{2}$ , where  $\varphi_i$  is the work function of the tip and sample. By filling this in in (2.4) and filling this in into the Ansatz for the wave function, we get

$$u_E(x) \propto \exp\left(\pm i \int^x d\xi \sqrt{\frac{2m}{\hbar^2} (E - \bar{\varphi})}\right). \quad (2.4)$$

If the energy  $E$  of the electrons is lower than the average work function of the materials of the tip and sample, we get

$$u_E(x) \propto \exp\left(\mp \int^x d\xi \sqrt{\frac{2m}{\hbar^2} (\bar{\varphi} - E)}\right) \quad (2.5)$$

$$= \exp\left(\mp \sqrt{\frac{2m}{\hbar^2} (\bar{\varphi} - E)} x\right). \quad (2.6)$$

Now in order to obtain the tunneling probability  $T(E)$  we use

$$\begin{aligned} T(E) &= \left| \frac{u_E(\Delta x)}{u_E(0)} \right|^2 \\ &= \exp\left(-2 \sqrt{\frac{2m}{\hbar^2} (\bar{\varphi} - E)} \Delta x\right). \end{aligned}$$

### 2.3 Simmons model

Combining the model from section 2.1 and the transmission probability of section 2.2, we can obtain the Simmons model in 3 dimensions[13, 14]. This model describes the IV characteristic of tunneling junctions and can be used to determine the average potential height. The model is given by

$$J(V) = \frac{e}{4\pi^2\hbar\beta^2\Delta x^2} \left( \bar{\varphi} \exp \left( -2\beta\Delta x \sqrt{\frac{2m\bar{\varphi}}{\hbar^2}} \right) - (\bar{\varphi} + eV) \exp \left( -2\beta\Delta x \sqrt{\frac{2m(\bar{\varphi} + eV)}{\hbar^2}} \right) \right) \quad (2.7)$$

In which  $J$  is the current density and  $\beta$  is a correction factor to correct for the integration of square roots. By taking the low voltage regime ( $eV \ll \bar{\varphi}$ ), the value of  $\beta$  is 1 and we can take the Taylor series of the square root around  $eV$  to obtain

$$\begin{aligned} J(V) &\approx \frac{e}{4\pi^2\hbar\Delta x^2} \left( \bar{\varphi} \exp \left( -2\Delta x \sqrt{\frac{2m\bar{\varphi}}{\hbar^2}} \right) - (\bar{\varphi} + eV) \exp \left( -2\Delta x \left( \sqrt{\frac{2m\bar{\varphi}}{\hbar^2}} + \sqrt{\frac{m}{2\bar{\varphi}\hbar^2}} eV \right) \right) \right) \\ &= \frac{e}{4\pi^2\hbar\Delta x^2} \left( \bar{\varphi} - (\bar{\varphi} + eV) \exp \left( -2\Delta x \sqrt{\frac{m}{2\bar{\varphi}\hbar^2}} eV \right) \right) \exp \left( -2\Delta x \sqrt{\frac{2m\bar{\varphi}}{\hbar^2}} \right). \end{aligned}$$

### 2.4 Inelastic electron tunneling spectroscopy

Inelastic electron tunneling spectroscopy is used in order to probe the vibrational states in a tunneling junction and can be used in order to probe the edge chemistry in a twisted edge junction. In IETS an IV curve is measured, for low biases, this curve is described by the Simmons equation as previously discussed. In this scenario only a single conduction channel is present. If vibrational modes are present in the junction, these modes can open an extra conduction channel through the junction where the electron will lose energy and excites the vibrational state[15, 4]. This is illustrated in figure 2.2a. This extra conduction channel increases the differential current  $\frac{dI}{dV}$  and will therefore be visible as a bump in the  $\frac{d^2I}{dV^2}$ . An idealized example of this is shown in figure 2.2b.

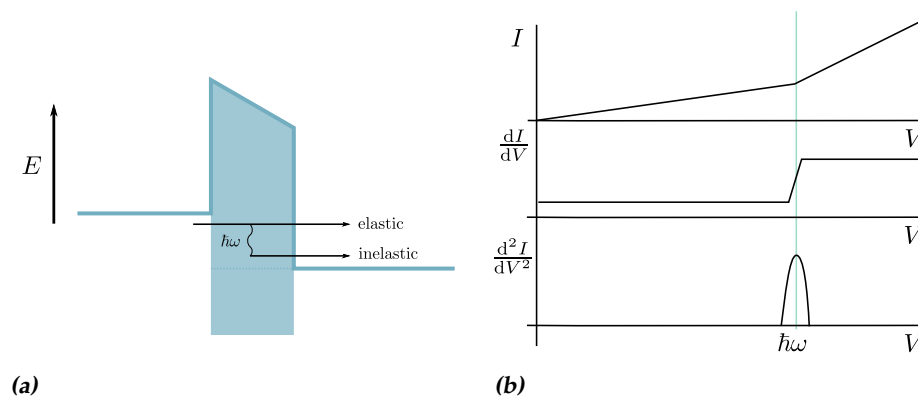


**Figure 2.2:** (a) Schematic overview of the tunnel junction. Besides elastic transport where the electron will keep its energy, also a second inelastic mode of transport becomes possible by a vibrational state. (b) IV curves obtained while performing IETS. At the energy  $eV = \hbar\omega$  a vibrational mode can be excited, causing an increase in the differential conductance. Figures adjusted from [4].

# Chapter 3

## Methods

During the project a scanning tunneling microscope (STM) was used to perform measurements. The main measurements are topographic data on gold on mica and highly ordered pyrolytic graphite (HOPG). This STM is described in section 3.1. In order to cool down the STM to liquid nitrogen temperatures (77 K), the STM is mounted in a dipstick that is directly inserted in a dewar filled with liquid nitrogen. This part of the setup, together with the vacuum system used, is described in section 3.2.

### 3.1 Scanning Tunneling Microscopy

The main technique used in this work is scanning tunneling microscopy (STM). In this surface technique, an atomically sharp tip is scanned across the surface. The typical distance between the tip and sample is on the order of Ångströms. This distance is kept constant using a feedback system based on the electrons tunneling between the tip and sample[16]. In section 2.1, the theory of electron tunneling is presented.

#### 3.1.1 Experimental setup

The STM used in the performed experiments, is a slider based design. This design is developed to be used in cryogenic environments. In the system, the tip is mounted to a slider that can be moved to adjust the height of the tip above the sample. The sample is mounted on an  $xy$  moving stage. Both the  $xy$  and  $z$  stage move by using piezoelectric actuators. The piezos used in the system are shear piezos and work by applying a high voltage to the piezoelectric material. This high voltage is provided by two high voltage amplifiers with a gain of  $G = 20$  and  $G = 25$ . By applying a bias between

the tip and the sample and measuring the current flowing through the junction, the separation can be calculated. For measuring the current, a femto DLPCA-200 current amplifier with a gain of  $1 \times 10^9 \text{ V A}^{-1}$  is used[17]. The distance between the tip and sample is kept constant using a feedback system. By recording the movements made by the tip during scanning, the topology of the sample can be measured. The scanning is done in two axes. The first axis is the fast moving axis which will be called the  $x$  axis. The second axis is the slow moving axis which will be called the  $y$  axis. By moving in a zigzag pattern, the sample is scanned. The surface is scanned two times along the fast axis. Both scans are taken in different direction and can therefore be used for studying the hysteresis in the system. The complete system is controlled by an SoftdB MK2-A810 which is an open source STM controller[18]. The computer used to capture the data and to control the STM controller is running an adjusted version of GXSM3 [19]. A complete schematic overview of the STM system can be seen in figure 3.1.

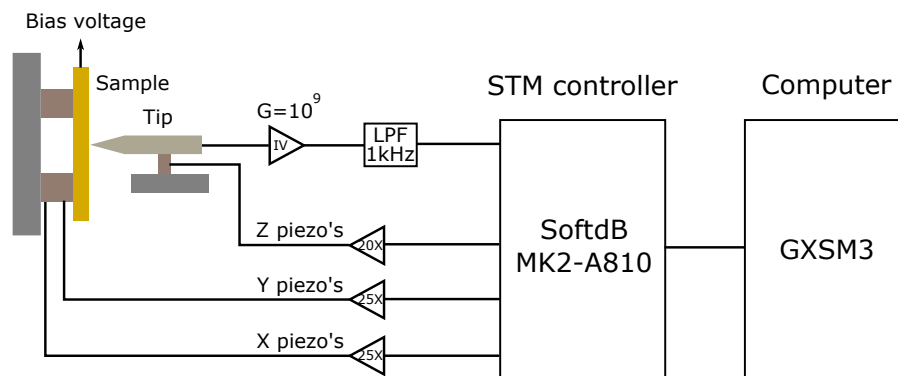


**Figure 3.1:** Schematic overview of the used STM system. On the left, the biased sample can be seen with the  $xy$  piezos that move the sample for scanning. Right to that the tip is shown that is attached to the  $z$  piezos and makes electrical contact to the current amplifier. The output of this amplifier is connected together with the signal of the piezo to the STM controller that handles the feedback and controls the scanning motion and data acquisition.

### Feedback system

In order to keep the tip at a constant distance from the surface of the sample, a feedback system is used. The STM controller contains the feedback system used for this. As an input for this feedback system, the current is measured and the current is amplified using a IV converter. In the controller, the logarithm of this current is calculated and the setpoint is subtracted to obtain the error signal. Using this error signal, the proportional

and integral feedback is calculated. A weighted sum of these signals is taken as the output signal. This resulting signal is amplified for the  $z$  stage piezo. This system is similar to the system discussed by Oliva et al.[20]

### Slip stick motion

The piezoelectric actuators used in the system have a range in the order of a  $3\ \mu\text{m}$ [21]. Therefore it is needed to implement a system to make coarse motion. In the STM used, this coarse motion is implemented using slip stick motion. By using the difference in friction between the piezo and a slippery surface when moving the piezos fast or slow, the object can be moved over macroscopic distances. In figure 3.2 this mechanism is demonstrated. The mechanism used for moving the tip in the  $z$  direction is described in a patent by Pan[22].

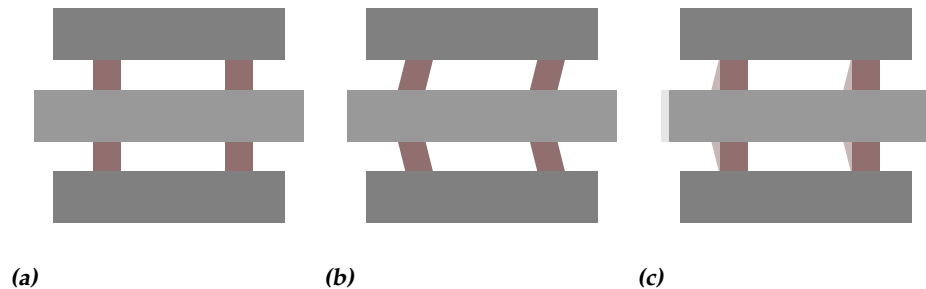


**Figure 3.2:** **a.** Initial position of slider (gray middle part) and piezos (brown parts). **b.** Position of slider and piezos after making the first fast movement of the piezos. Note that the slider is not moved due compared to the first image. This is the slip motion. **c.** Slow recovering of the piezos moving the slider further. This is the stick motion of the slip stick mechanism. The previous position is shown as a light image.

### 3.1.2 Data analysis of STM images

In order to calibrate the STM system, the data needs to be analyzed and some measurement artifacts need to be corrected in order to retrieve the most optimal results. The main artifacts considered are the misalignment between different rows, piezo hysteresis and a plane offset. Software was written in Python in order to correct these artifacts.

### 3.1.3 Fast axis misalignment correction

In the setup used, the piezos that move the  $z$  stage are also used to make the course movements of the  $z$  stage. This means that in certain scans, the height of two adjacent lines can be different due to slipping of the movement stage. In order to correct the misalignment between adjacent rows

along the fast axis, the difference between multiple lines is determined. This is done by subtracting the height of two adjacent lines and finding the median difference. The median difference is then subtracted from the second line. By doing this for the entire image, all the lines are positioned at the same height. An example of this process is shown in figure 3.3.

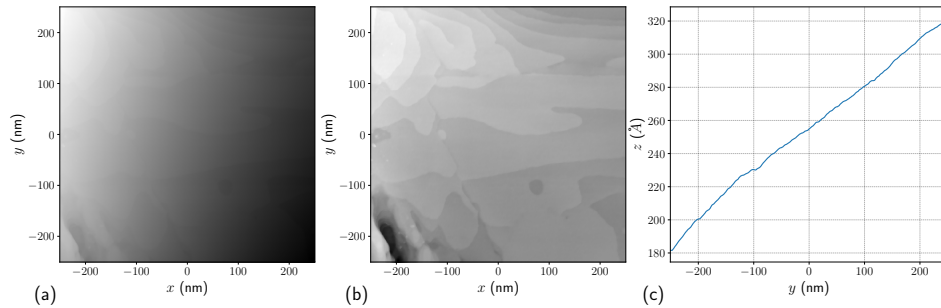


**Figure 3.3:** *a.* Rough data as captured using the STM. *b.* Corrected image after subtracting the median difference between two lines. *c.* Line cut through the removed background as a function of the vertical pixel index.

### 3.1.4 Piezo hysteresis correction

The  $xy$  stage of the microscope is moved by using shearing piezo electric actuators. These attenuators work by the inverse piezo electric effect where a material deforms after applying an electric bias[23]. Using piezoelectric actuators enables control of the stage on the nano scale. One of the disadvantages is the hysteresis present in the shear voltage dependency [24, 25]. This can be clearly seen in the line cuts of the scan and rescan along the fast axis of the microscope. A typical example of this phenomenon can be seen in figure 3.4. In the system used, this hysteresis is particularly noticeable.



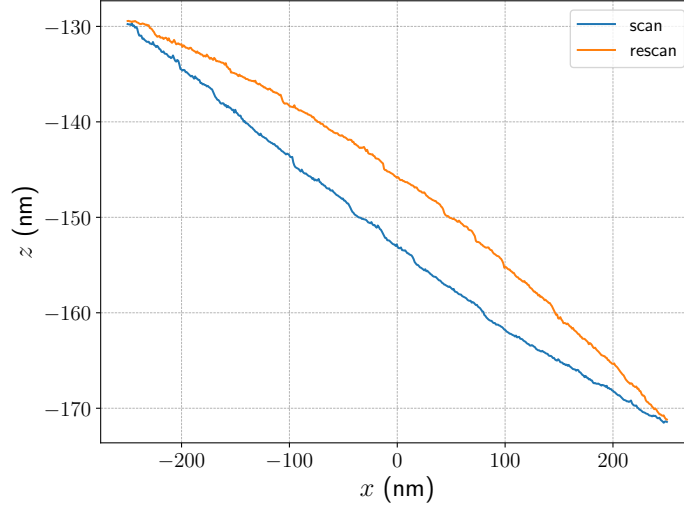


**Figure 3.4:** Example of the a line cut of a measurement of gold on mica at room temperature. The hysteresis is clearly visible as both scans are disconnected, but both share the same features.

The correction of the hysteresis is made by using a moving window correlation method as also demonstrated by Fu et al [26]. By taking a small area around a point at coordinate  $x$  and sliding this over the  $x$  axis, we can find the position where the difference between the trance and retrace of the images is the smallest. The distance where the difference is minimal, is taken as the piezo hysteresis. This can be described as

$$\Delta x(x_p) = \arg \min_{\Delta x} \sum_{i=-\frac{N}{2}}^{\frac{N}{2}} (z_S(x_p + i + \Delta x) - z_R(x_p + i))^2, \quad (3.1)$$

where  $\Delta x$  is the piezo hysteresis,  $x_p$  is the position on the fast axis measured in pixels,  $N$  is the window size and  $z_S$  ( $z_R$ ) is the height measured during the scan (rescan). Through this measured hysteresis, a polynomial model is fitted. The difference  $\Delta x$  of this fitted model is divided by 2 and the fast axis of the image are adjusted. An example plot of  $\Delta x$  and the resulting line cut is shown in figure 3.5.

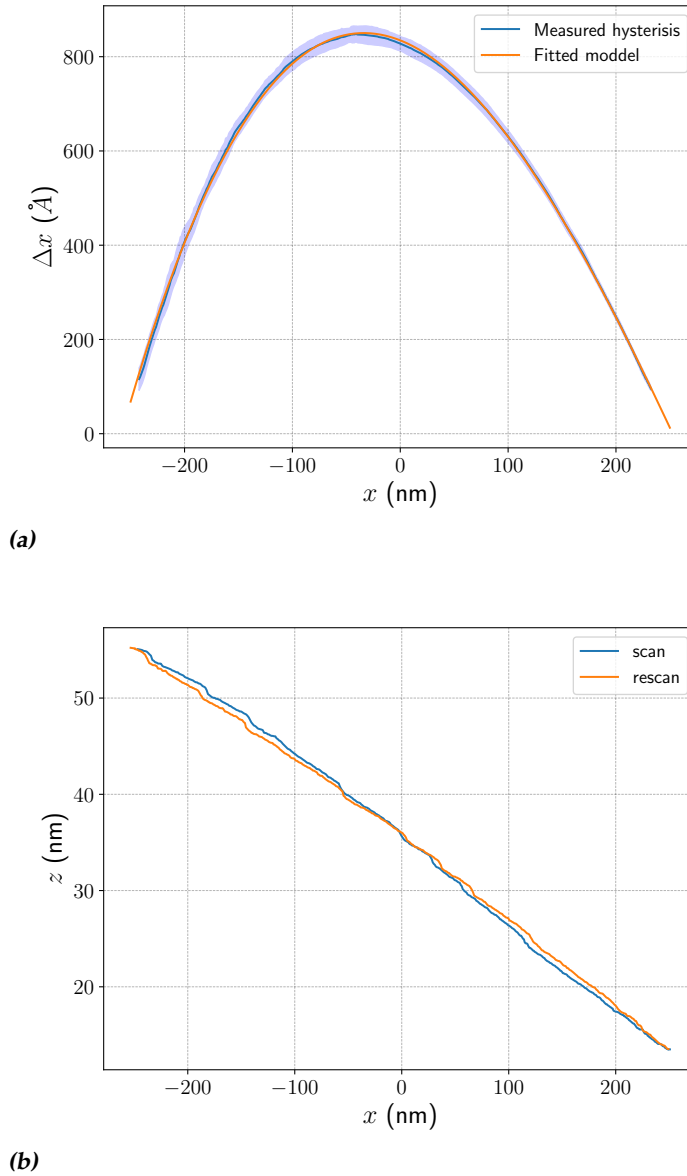


**Figure 3.5:** (a) Measured  $\Delta x$  for the data set presented in figure 3.4, the error is determined by taking the standard deviation along all the lines. The orange line is the fitted model through the data. (b) same line as shown in figure 3.4, but now after the correction is applied.

After correcting the axes, the measured data can be resampled using the

new axes and bilinear interpolation by using

$$z(x, y) \approx \frac{1}{(x_2 - x_1)(y_2 - y_1)}. \quad (3.2)$$

$$\begin{bmatrix} z(x_1, y_1) \\ z(x_1, y_2) \\ z(x_2, y_1) \\ z(x_2, y_2) \end{bmatrix}^T \begin{bmatrix} x_2 y_2 & -y_2 & -x_2 & 1 \\ -x_2 y_1 & y_1 & x_2 & -1 \\ -x_1 y_2 & y_2 & x_1 & -1 \\ x_1 y_1 & -y_1 & -x_1 & 1 \end{bmatrix} \begin{bmatrix} 1 \\ x \\ y \\ xy \end{bmatrix} \quad (3.3)$$

where  $z(x, y)$  is the topographic height at the position  $x, y$ ,  $x_1, x_2$  are the nearest coordinate on the  $x$  axis on the original grid and  $y_1, y_2$  are the nearest coordinates on the  $y$  axis of the original grid. [27, 28].

### 3.1.5 Plane correction

As samples will not be mounted perfectly perpendicular compared to the  $xy$  plane, all images will have a linear plane offset. In order to correct this, the sample data has a constant plane subtracted from it. This plane should be chosen in such a way that the terraces measured, are aligned to the  $xy$  plane of the STM.

The normal of this plane is determined by finding the most common normal in the image. To find this vector, first all the normal vectors of the topology are found using a down sampled topographic image. Using all these vectors the most likely values for all the components are found. This is done by finding the maximum of a histogram of all the values of a component of the normal vectors in the measurement. Subsequently a flat plane with this most common normal vector is subtracted from all the measured heights. In figure 3.6 a 3D view of a flattened image is shown.

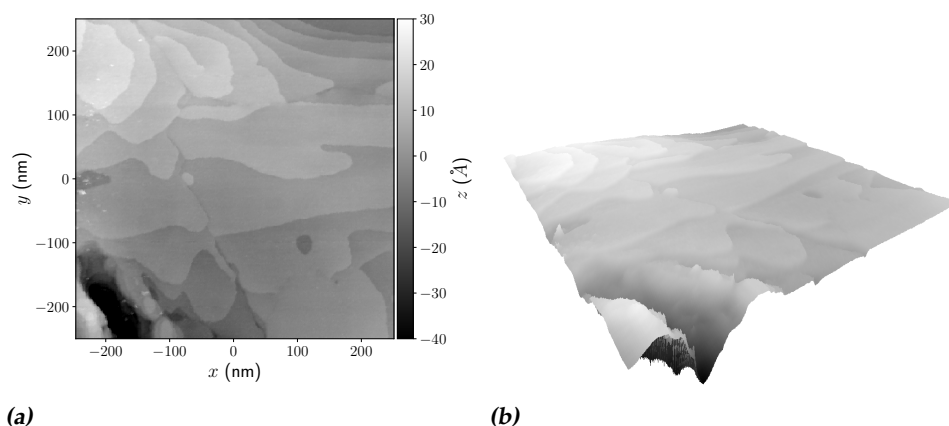


**Figure 3.6:** **a.** False color plot of a typical flattened image of gold on mica taken at room temperature. **b.** Same image but now rendered in 3D, showing the relative flatness of the terraces in the measurement.

## 3.2 Vacuum and cryogenic system

In order to perform cryogenic experiments, the STM head with the  $xy$  stage and  $z$  stage are mounted in a dipstick. This dipstick is a large tube that can be inserted in a nitrogen or helium dewar. Before inserting the dipstick in a dewar, it is needed to pull the dipstick to a vacuum. In order to do this, a Pfeiffer HiCube pumping system is used. This system contains a membrane pre-pump and a turbo pump. After inserting the dipstick in the cryogenic liquid, the cool-down will pump down the system even further using cryo-pumping.

The dipstick needs to be pulled vacuum on a table before inserting in the dewar. After a sufficient vacuum is reached, the pump is disconnected and the dipstick can be inserted into the dewar. During the insert, the dipstick can be further pumped vacuum using a vacuum hose to connect the pump to the dipstick.

Figure 3.7 contains a simplified schematic of the used system.

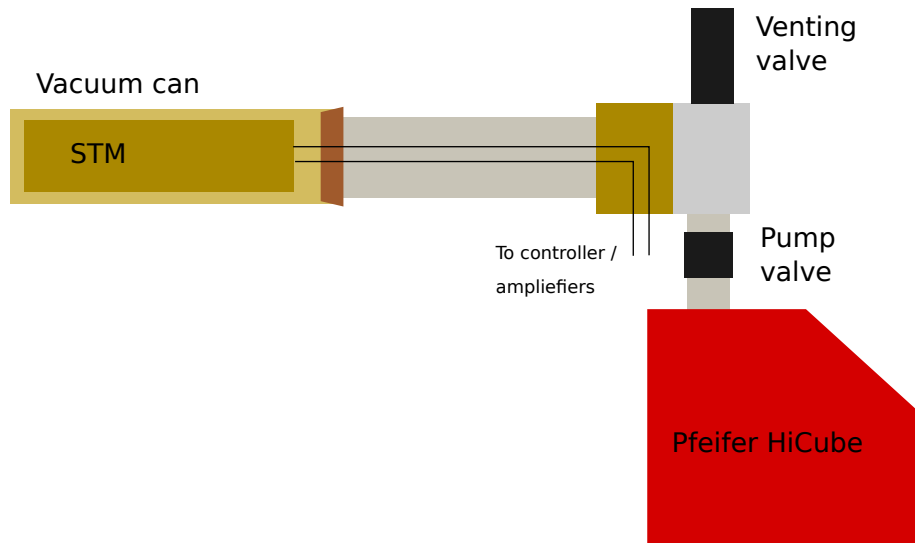


**Figure 3.7:** Simplified schematic overview of the main parts of the dipstick with the vacuum system. On the left the vacuum can at the end of the dipstick is shown that contains the STM. With a conical seal, this can is sealed. The dipstick contains the wires for the STM. At the other side of the dipstick the connections to the STM are made. This side also contains the venting valve for venting the system. Also the Pfeifer vacuum pump is connected to this side of the dipstick via a pump valve.

# Chapter 4

## Results

Various experiments were conducted using the STM setup. Electrochemically etched nickel tips were used for all experiments conducted. The tips are etched using a solution of 2M KCl using an gold ring as a second electrode. A sinusoidal wave with a frequency of 20 Hz a peak to peak voltage of 6 V and an offset of 3 V were used. To the tips a small weight was attached to make sure that the tips fell after etching. This process is comparable to a process described by Cavalini et al [29].

### 4.1 Gold on mica samples at room temperature

In the following section we will discuss the results obtained using the setup in ambient conditions. The first samples that were used in order to condition the tips of the STM, are gold samples grown on mica. The gold on these samples is a layer of Au(111) with atomic flat areas with atomic steps[30, 31]. These samples are commonly used for tip preparation and z stage calibration.

#### 4.1.1 Typical images

For the most data that was obtained, there were clear atomically flat surfaces visible with atomic steps between the surfaces. The resolution and quality of these images varied widely mainly depended on the quality of the tip that was in use at that moment. Figure 4.1 shows a comparison between typical, good and the best data obtained on the system.

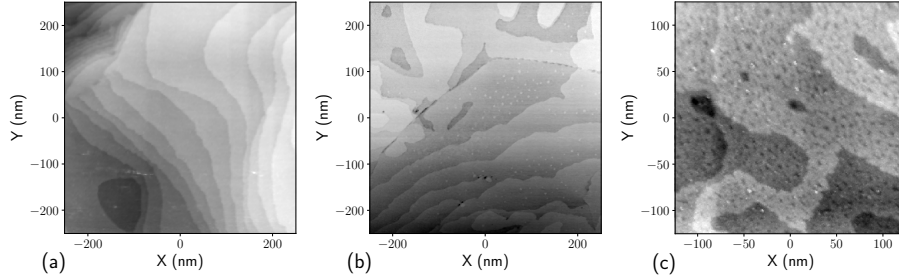


**Figure 4.1:** Three examples of obtained results using the STM setup. **(a)** Typical result obtained using the setup. Terraces are visible and the data can be used to obtain  $z$  stage calibrations. **(b)** Good data obtained using our setup. In this image, more details can be seen. **(c)** Best result obtained using our setup. Notice the small holes in the surface. Please note that the scale on the last image is different compared to the first two images.

#### 4.1.2 Piezo hysteresis correction

For the data obtained, it is tried to correct the piezo hysteresis. This correction was successful for all the measurements except for the data obtained on the 29 of June. Therefore, the uncorrected data is used for the further analysis of this experiment. A third order polynomial  $\Delta x(x) = ax^3 + bx^2 + cx + d$  is fitted to the data. The obtained parameters for the fits are listed in table 4.1. There is some variation of the obtained parameters between the different measurements, however all the fits are similar. An overview of the final fitted functions can be found in figure 4.2

Dataset	$a$ ( $\text{\AA}^{-2}$ )	$b$ ( $\text{\AA}^{-1}$ )	$c$	$d$ ( $\text{\AA}$ )
2022/05/30	$9.5(1) \times 10^{-9}$	$-1.143(2) \times 10^{-4}$	$-5.84(5) \times 10^{-2}$	$7.0(4) \times 10^2$
2022/06/29	$6.2(3) \times 10^{-9}$	$-1.090(6) \times 10^{-4}$	$-4.5(1) \times 10^{-2}$	$6.92(1) \times 10^2$
2022/07/07	$1.268(9) \times 10^{-8}$	$-1.371(1) \times 10^{-4}$	$-9.03(3) \times 10^{-2}$	$8.347(3) \times 10^2$
2022/07/12	$6.7(9) \times 10^{-9}$	$-1.078(1) \times 10^{-4}$	$-4.93(4) \times 10^{-2}$	$7.110(3) \times 10^2$
2022/06/28	$3.5(2) \times 10^{-8}$	$-1.41(1) \times 10^{-4}$	$-5.9(2) \times 10^{-2}$	$2.32(1) \times 10^2$

**Table 4.1:** Fit parameters found by fitting the shift caused by piezo hysteresis to a third order polynomial. The top four measurements consist of measurements over a range of 500 nm. The last measurement is over a range of 250 nm.

#### 4.1.3 $z$ stage calibration

It is possible to obtain a calibration of the  $z$  stage using a flat image. In order to do this, a step of an image is taken and a histogram around this

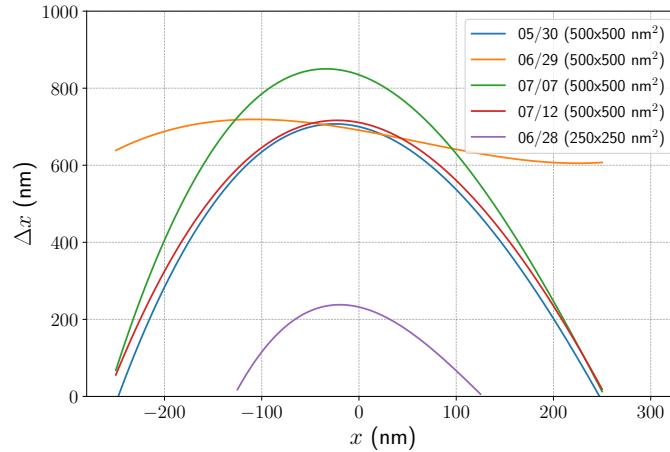


**Figure 4.2:** Results of fitting the piezo hysteresis for the various data sets. Note that the curve for the data set of the 29th of June is different compared to the other data sets. This is due to the correction procedure not working correctly for this data set. The original uncorrected data is used for the rest of the analysis.

area is made. Another possibility is to use a line cut through the image to measure the height of the terraces.

We compared both methods by taking data obtained on multiple days and comparing the obtained results. The first method is by taking histograms. For 5 data sets flat areas were chosen and histograms were made. Areas where chosen where a clear and single step could be identified. From these histograms, Gaussian fits were made from the peaks and height data extracted from this histogram. After this, also the height difference between two terraces is measured by using a line cut. The line cuts are made through roughly the same area used for the histogram. In order to filter out some of the noise, the line cut is averaged over a width of 5 nm. The data for one of the measurements is shown in figure 4.3. For the other used data sets, similar figures are shown in appendix A.



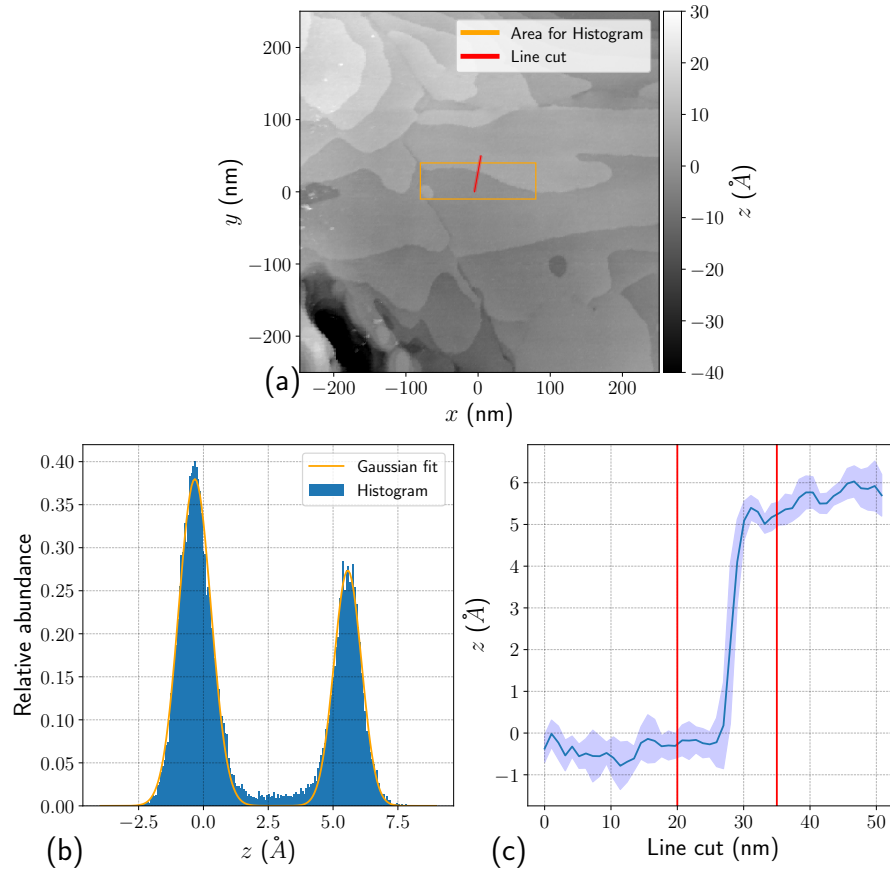


**Figure 4.3:** (a) Image of the measurement used for the data analysis. In orange the area used for making the histogram in b is shown. In red the line for the line cut is shown. The width of the red line is the width used for averaging the data for the line cut. (b) Histogram of the orange region shown in the first image. The blue bars give the measured data. The orange line is the fit of two Gaussian functions made to this data. (c) Data of the line cut shown by the red line in the first figure. The blue line is the average height around along the width of the line, the light blue area is the standard error on this value. The red lines indicate the points where the height is determined for finding the terrace height.

The data for all the data sets is shown in figure 4.4. Here the different apparent (before calibration) heights between two terraces are shown. Both the histogram and the line cut method give comparable results that always fall within a single error bar. The absolute value of the height difference varies

between samples. By taking the weighted average, the resulting apparent height between two terraces is  $4.6(3)$  Å by using the histogram method and  $4.9(3)$  Å with the line cut method. In combination with the know value of  $2.4$  Å for terrace height, we find a correction value for the  $z$  axis[32].

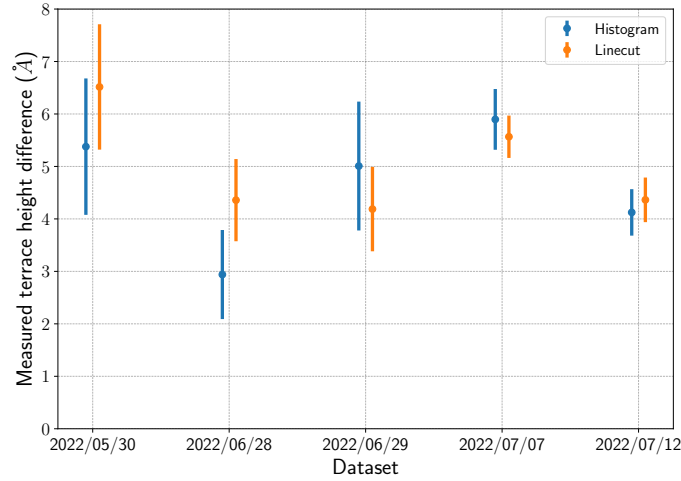


**Figure 4.4:** Comparison for the apparent terrace heights for multiple data sets. The data obtained by using a histogram is shown in blue. The data obtained using line cuts is shown in orange.

#### 4.1.4 IZ curves

Besides the topographic images, also the current as a function of the separation from the surface is measured. To do this the  $z$  is varied and the current is recorded. The contact point ( $z = 0$  above the surface) is determined by the first point where the current is above  $9.9$  nA. This is not the point where the tip actually touches the surface, but this point is close to the maximal current ( $10$  nA) measurable with the used current amplification. During the IZ measurements, the contact point changes slightly. This is likely due to the tip changing when making contact. A typical IZ curve is shown in figure 4.5. An exponent in the form of

$$I(z) = I_0 \exp(\kappa z)$$

is fitted to the measurement data as the transmission probability decreases exponentially as described by equation (2.7). In this formula,  $I(z)$  is the current at a distance  $z$ .  $I_0$  is the current at  $z = 0$  and  $\kappa$  is the decay constant for the current. By taking the weighted average over multiple fitted curves, we find  $\kappa = 0.44(8)$  nm<sup>-1</sup>

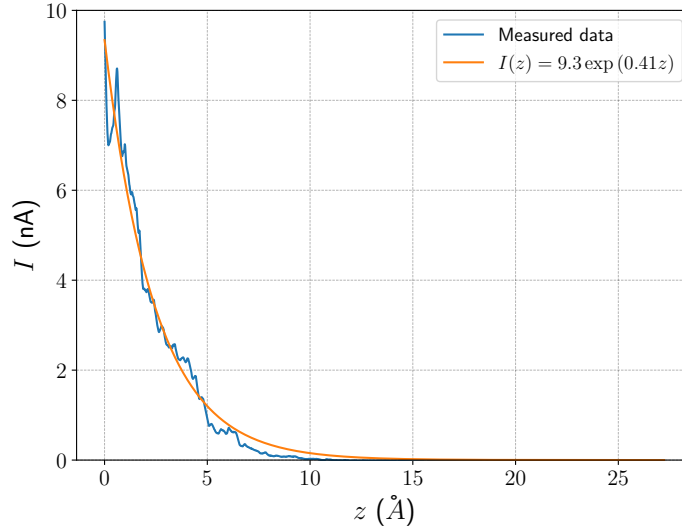


**Figure 4.5:** Current as a function of the tip separation from the point where the current is 10 nA. In blue the measured data is shown, in orange the fitted exponential decay.

## 4.2 HOPG samples at room temperature

Besides gold on mica, also highly ordered pyrolytic graphite (HOPG) samples were measured. These graphite samples consist of highly ordered graphene layers and atomic HOPG is widely used in scanning probe microscopy in order to calibrate  $x$ - $y$  stages [33, 34].

Before measurements were made on HOPG, the tip was conditioned on a gold surface. The surface of HOPG was exfoliated before measurement to ensure a clean graphite surface. Typical surfaces of HOPG are flat compared to the gold samples. A typical result is shown in figure 4.6.

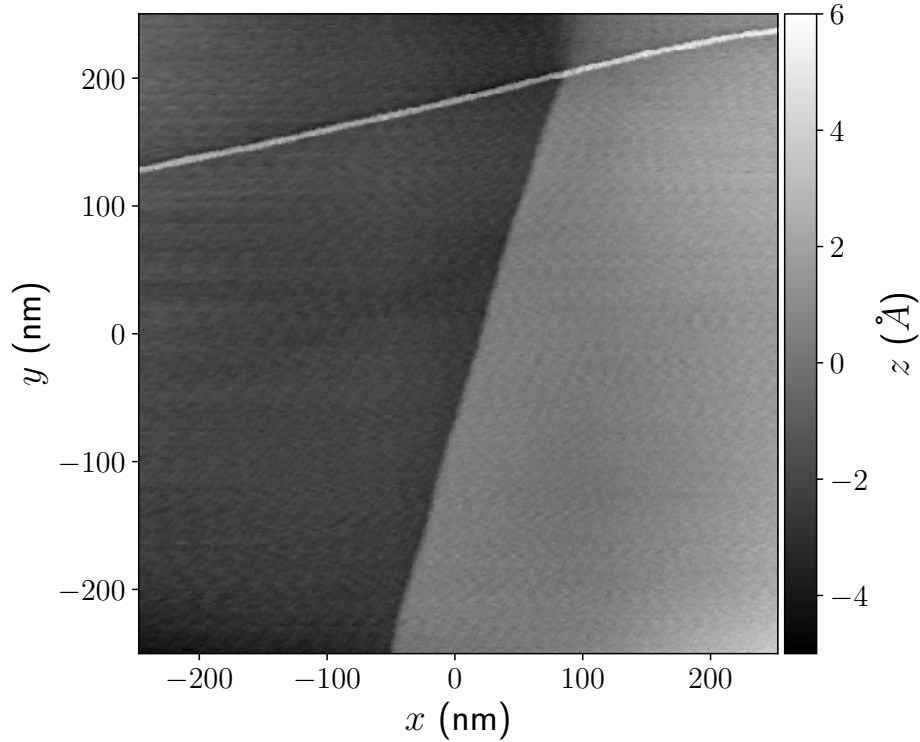


**Figure 4.6:** Example of a flake of HOPG measured in the STM. Two different flakes can be seen on the bottom. On the top there is a different structure divided by a high line.

#### 4.2.1 Height of flakes

Similar to the height differences of terraces that were measured for gold, we can also measure the height of the flakes in the image. Both the histogram and line cut method can be used to find the height again. In figure 4.7 the data analysis is shown. For the data set shown a height of  $2.5(5)$   $\text{\AA}$  for the histogram method and  $3.1(2)$   $\text{\AA}$  for the line cut method.

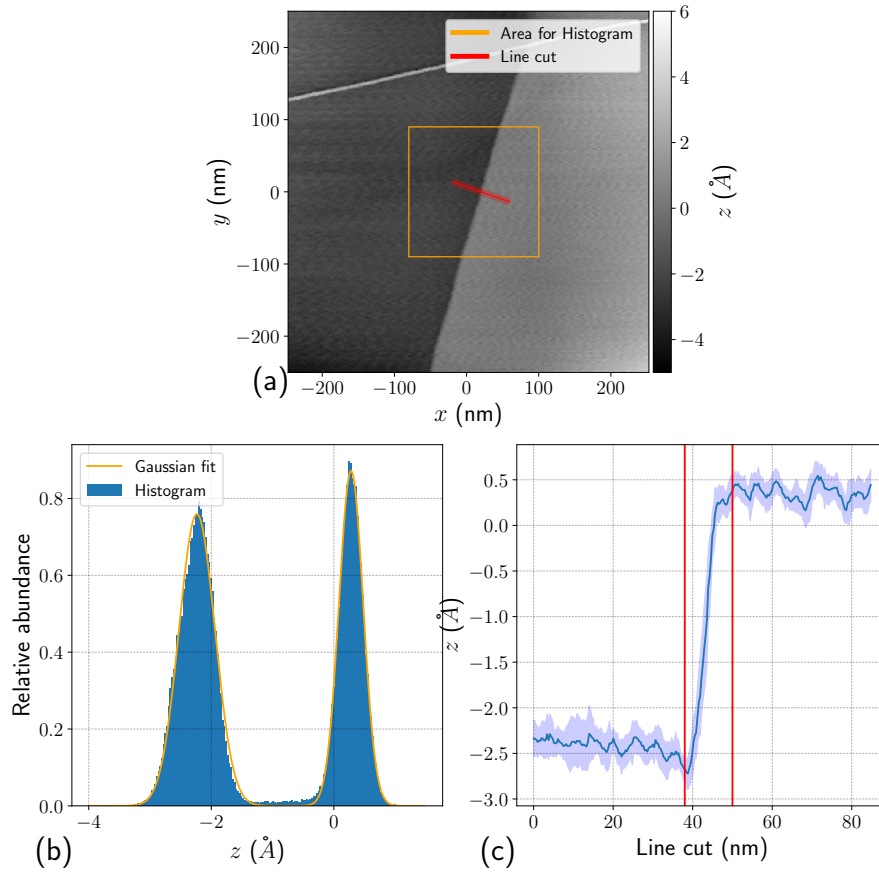


**Figure 4.7:** (a) Image of the measurement used for the data analysis. In orange the area used for making the histogram in b is shown. In red the line for the line cut is shown. The width of the red line is the width used for averaging the data for the line cut. (b) Histogram of the orange region shown in the first image. The blue bars give the measured data. The orange line is the fit of two Gaussian functions made to this data. (c) Data of the line cut shown by the red line in the first figure. The blue line is the average height around along the width of the line, the light blue area is the standard error on this value. The red lines indicate the points where the height is determined for finding the terrace height.

## 4.3 Gold on mica samples at liquid nitrogen temperature

After tip preparation was performed on gold on room temperature to ensure a good tip and sample, the dipstick was cooled down. The system was allowed to come to an thermal equilibrium before measurements were started.

### 4.3.1 Problems during cooldown

Measurements were attempted at liquid nitrogen temperatures (77 K). Most measurements of gold on mica did not result in the same kind of terraces as seen in the measurements made at room temperature. Even after dipping and pulsing the tip, the surface would not give the expected terraces as measured at room temperature. After warm up the tip and sample would give the same results as before the cool down.

#### Heater

In order to prevent condensation, a heater was mounted to the sample. In the first iteration, the heater (a 5.6 k $\Omega$  resistor) was mounted to the side of the sample. Using this iteration the data shown in figure 4.11 was measured. The usability of this heater was limited due to the solder used to connect the heating resistor, melting during the heating. A second sample used a heater mounted below the sample. The wires were soldered to the resistor, but also covered with an isolating epoxy that is primarily used to fix the sample to the heater. This sample was heated during the cool down by applying a voltage of 70 V.

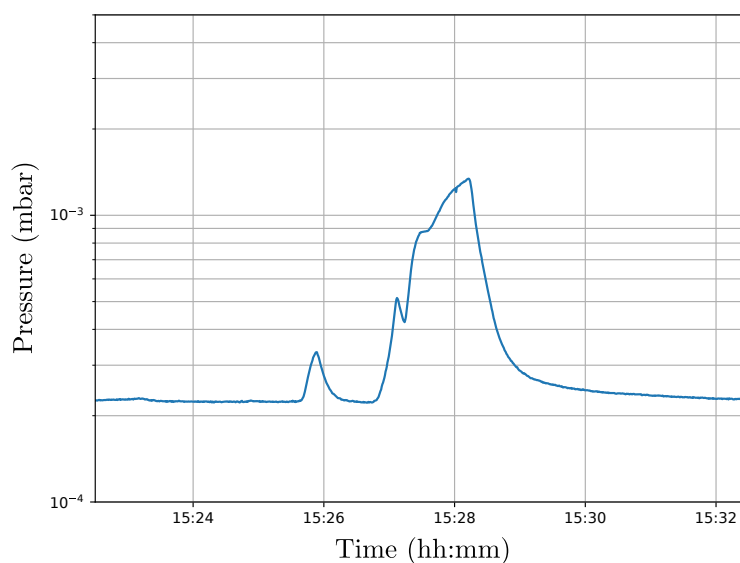
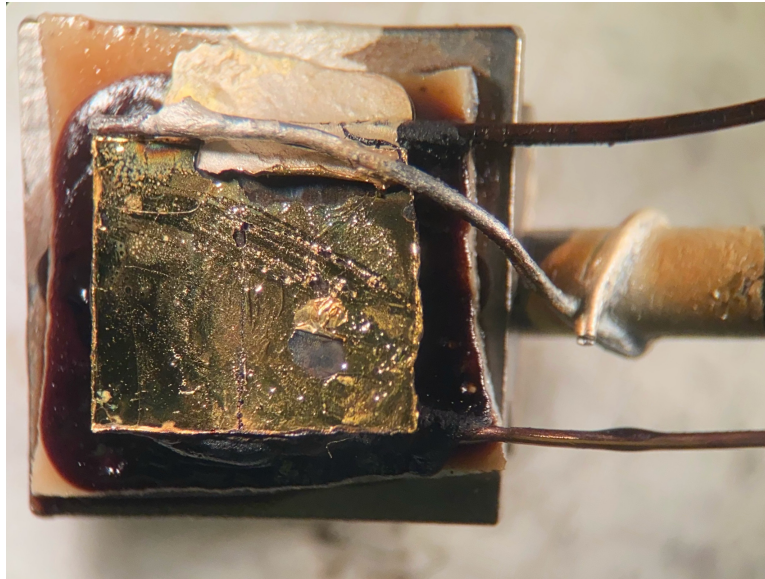
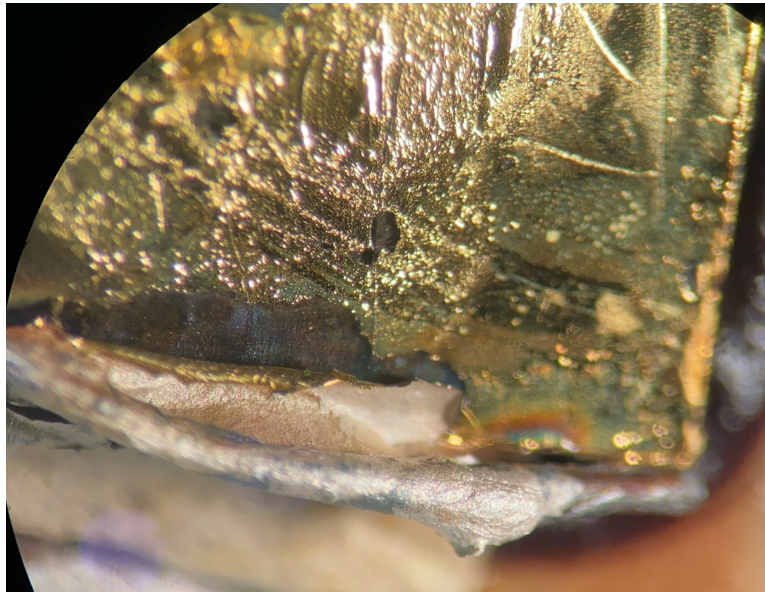


**Figure 4.8:** Pressure in the system while the heater was turned on. During the small peak, the heater was first turned off after the pressure started to rise. The big peak was during heating of the sample. The pressure returned to the base pressure by itself.

Initial results after heating did not give satisfactory results, the sample was heated by applying the highest voltage possible with the system (200 V). During this heating, the pressure at the top of the dipstick rose rapidly as demonstrated in figure 4.8. After the pressure was recovered and the tip was approached again, the tunneling junction was not stable anymore. Suspected is that during this peak, the sample and heater were heated too much and burned. The resistance of the heater remained constant after this heating, indicating that the contacts to the heater kept in place. After heating the system back up to room temperature the sample seemed heavily damaged as is shown in figure 4.9.



(a)



(b)

**Figure 4.9:** (a) Microscopic photograph of the damaged gold sample. A clear discoloring around the sample holder and damage to the sample can be seen. (b) Close up of the gold sample near the wire connecting the sample to the sample holder. Delamination of the sample is visible next to discoloring of the sample.



### 4.3.2 $z$ stage calibration

It can be expected that the response of the piezos is different at low temperatures compared to room temperature. Therefore it is important to recalibrate the STM system at low temperature. Unfortunately, only a single measurement with identifiable terraces at 77 K was obtained. An image of this data are shown in figure 4.10.

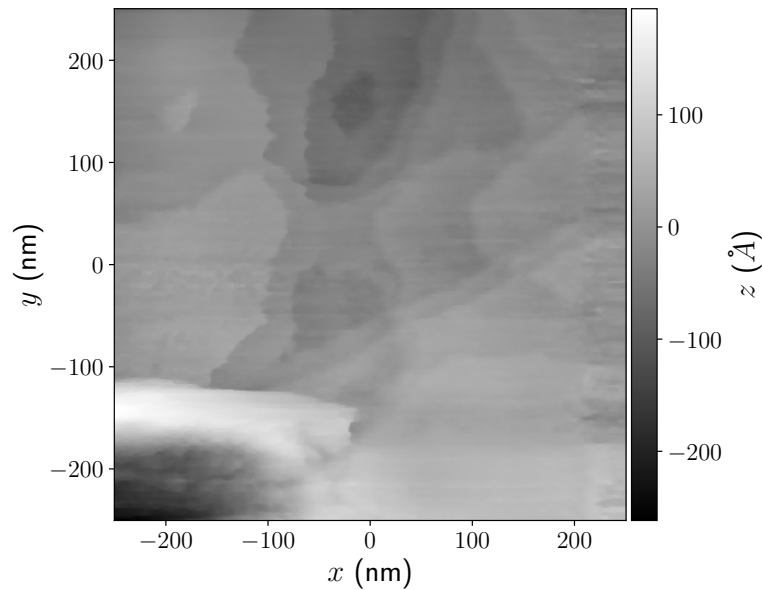


**Figure 4.10:** Data of gold on mica obtained at 77 K. Terraces are visible that can be used to perform the  $z$  stage calibration. Clear measurement artifacts are visible in this measurement.

Using this measurement an estimation of the calibration can be made. The results of this measurement is shown in figure 4.11. Due to the large measurement artifacts present in this measurement, the procedure used for flattening the data did not work as well on this data compared to the data at room temperature. Therefore the peaks in the histogram are widened a lot and it is hard to find the peak height belonging to the two terrace heights. This is also visible in the line cut where it is clear that the terraces are not flat. The obtained apparent heights using the two different methods are  $12(4)$  Å for histogram method and  $16(3)$  Å for the line cut method.

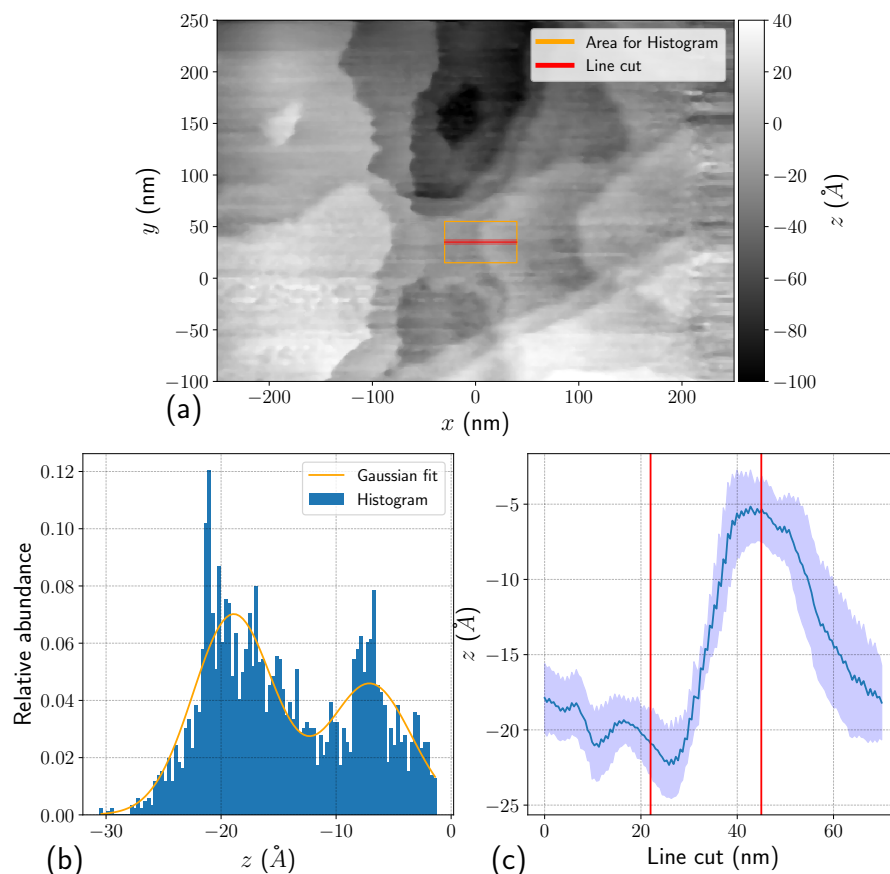


**Figure 4.11:** (a) Image of the measurement used for the data analysis. In orange the area used for making the histogram in b is shown. In red the line for the line cut is shown. The width of the red line is the width used for averaging the data for the line cut. (b) Histogram of the orange region shown in the first image. The blue bars give the measured data. The orange line is the fit of two Gaussian functions made to this data. (c) Data of the line cut shown by the red line in the first figure. The blue line is the average height around along the width of the line, the light blue area is the standard error on this value. The red lines indicate the points where the height is determined for finding the terrace height.

### 4.3.3 IZ curves

Similar to the gold samples at room temperature, also the IZ curves were measured at 77 K. The curves deviate less from an exponential decay compared to the similar curves taken at room temperature. By taking the weighted

average we obtain a decay constant of  $1.7(3) \text{ \AA}^{-1}$ . It should however be noted that although this value is different compared to the value obtained in section 4.1.4 the decay constant is very similar before applying the  $z$  calibration.

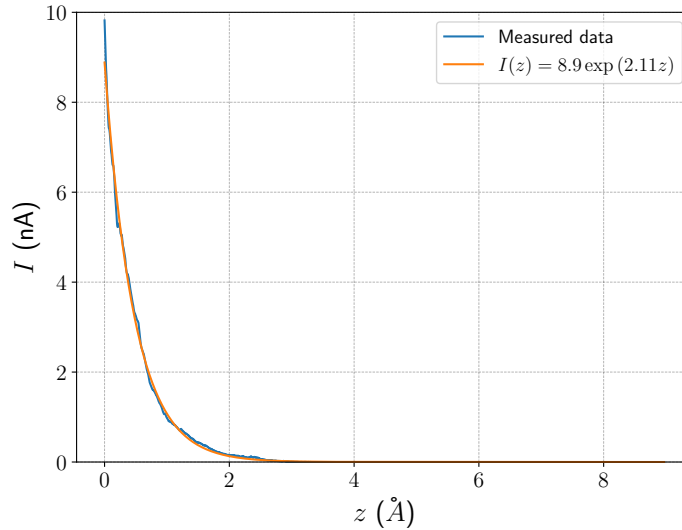


**Figure 4.12:** Current as a function of the tip separation from the point where the current is 10 nA. In blue the measured data is shown, in orange the fitted exponential decay.

#### 4.4 HOPG samples at liquid nitrogen temperature

Besides Au on mica, also HOPG samples were measured under cryogenic conditions. Just like the cryogenic experiments for gold, these experiments did not yield the results that would be expected from these samples. The measurements contain large rounded features. These features are consistent between scans, however they are not what you would expect from HOPG samples. A typical example of the data obtained is shown in figure 4.13.

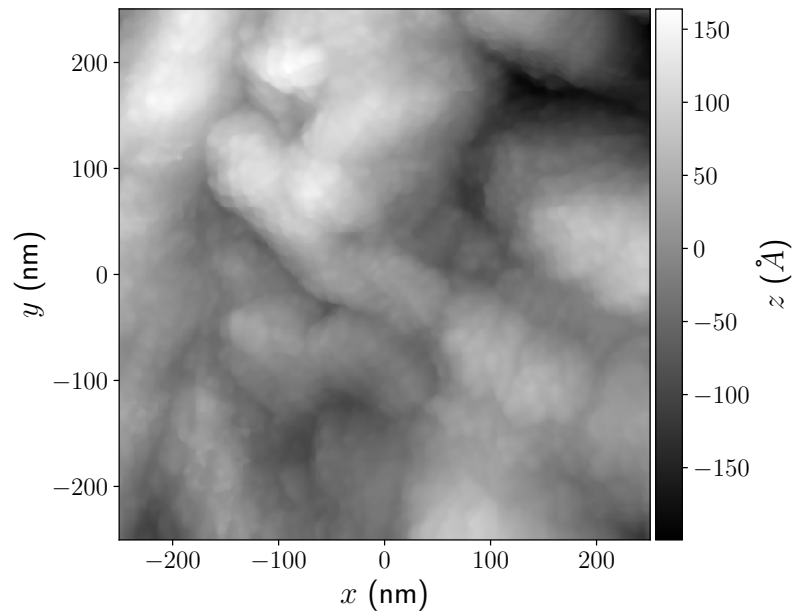


**Figure 4.13:** Typical result obtained for an HOPG sample at 77 K. The topography measured is more textured compared to the really flat surface of HOPG measured at room temperature.

## Discussion and Outlook

In this work we discussed the measurement and calibration of the STM set up. Due to time constraints it was not possible to implement IETS anymore. In section 5.3 a proposal for implementing this set up is discussed.

### 5.1 Calibration and measured samples

Using Au on mica the  $z$  stage of the STM setup is calibrated. For the data in this study, many different tips and samples were used. In figure 4.4 the measured apparent height of the step edges do vary between samples. Furthermore, both methods used, resulted in large uncertainties in the step height. This error also propagate in the measured values of for instance the decay constant in the  $I_Z$  curves.

In using the histogram method, the main contributor to the error in the apparent step height is the width of the Gaussian peaks in the height histogram. Not only the natural variation of the height in the sample causes this widening, also the quality of the data processing plays a large role. The better the image is flattened, the smaller the variation in the histogram will be, giving better calibration values. The line cut method relies on the user to determine where in the line cut both terraces are sampled. This is less reproducible compared to function fitting. Furthermore, near the edge of a terrace, the feedback can overreact to sharp features, distorting the line cuts through the edge. In order to better determine the calibration value, fitting a plane though both terraces could potentially yield better results.

In the measured HOPG sample, the steps measured in section 4.2 are smaller than compared to previous reported[35, 36]. It is suspected that this difference can be contributed to errors in the calibration of this STM. More mea-

measurements and calibration steps should be taken in order to measure the step height in HOPG.

### 5.1.1 Correction for piezo hysteresis

At room temperature, the piezo hysteresis is large and noticeably deforms the data obtained using the setup. In most images, the described method for correcting this hysteresis worked well. All the obtained fits for  $\Delta x$  are similar between data sets. The larger difference between the hysteresis of the data obtained on the 7th of July and the other dates might be attributed to differences in scan speeds since larger scan speeds cause larger hysteresis[37]. Further research with varying scan speeds could be performed in order to obtain calibration curves for this system. A parabolic model is previously shown to describe the hysteresis well[27]. This is different compared to our results where a third order polynomial described the hysteresis better. The main reason for this difference could be the asymmetrical behavior in the piezo hysteresis and therefore a model with an odd primary term being the best fit.

When applying the used moving window correction method, it is not possible to separate the hysteresis on the fast moving  $x$  axis and the  $z$  axis. It is expected that the hysteresis in the  $z$  axis is negligible due to the much smaller moving range of the  $z$  piezos compared to the  $x$  piezos.

### 5.1.2 IZ curves

IZ curves were measured at room temperature and 77 K for gold samples. Comparing the curves obtained at room and cryogenic temperatures, it can be seen that the curves at 77 K better follow the exponential curve. This shows that the stability of the STM system at low temperatures is much higher compared to the stability at room temperature. The found decay constants are different for room temperature and cryogenic temperature. This can be caused by a layer of condensation on the sample. By using the Simmons model and fitting this to an IV curve, this can be verified.

## 5.2 Improvements to improve cryogenic performance

During the experiments performed, it is clear that the performance of the STM during cool down is not yet enough for reliably performing topographic measurements and IETS. The main problem limiting cryogenic measurements is the contamination of the sample and tip. This contamination is most likely in the form of condensation left over gas remaining from pumping the system to a vacuum. A prime candidate for this gas is oxygen which has a boiling point of 90 K. Because the tip and sample work again

after heating the system back to room temperature, the contamination is most probably an atmospheric gas at room temperature. Using a heater in order to clean the sample had some effect, however the heater failed, by either melting the solder that connects the heater or damaging the sample by overheating, too quickly in order to have a long time where the system is clean.

Furthermore, the heating of the sample is hard to control due to not knowing the temperature of the sample. For further experiments, it might be beneficial to redesign the sample holder in order to accommodate a heater and thermometer directly under the sample like previously used by Nathanael van den Berg for twisted edge junctions[38]. Using epoxy to mount the heater and wires, enables the heater to become hotter than the melting point of solder. This gives access to the possibility to anneal the sample in the system[39]. By also having a thermometer under the sample, the sample could be kept at a constant predetermined temperature. This would have prevented the damage as discussed in section 4.3.1

Further improvements to the cryogenic performance could possibly be made by lowering the pressure in the dipstick during insertion. This could be obtained by remounting an ion pump and cleaning and performing a full bake out of the system. The ionic pump was removed from the setup since this pump did not function anymore. It could be expected that ensuring a lower starting pressure lowers the amount of material able to condense on the sample or tip. This, in combination with the heater, could improve the chances to obtain good images.

### 5.3 Inelastic Electron Tunneling Spectroscopy

In order to perform IETS in the current setup, only minor changes to the setup need to be made. To measure the differential conductivity  $\frac{dI}{dV}$ , the bias voltage across the junction is modulated with a small AC voltage. Measuring the amplitude of the AC current gives a direct measure for the differential conductivity[4]. By numerical differentiation,  $\frac{d^2I}{dV^2}$  can be found. These measurements can be performed using a lock-in amplifier[40]. For the small AC voltage needed to modulate the bias, the local oscillator of the lock-in amplifier is used. The input side of the lock-in needs to be AC coupled to the amplified current.

The schematic in figure 3.1 needs to be adapted to incorporate this change. This new set-up is shown in figure 5.1. When first implementing this system, it is important to carefully consider the frequency the measurement is made. Important factors to consider, are the signal to noise ratio of the AC bias, the parasitic capacitance of the STM and the bandwidth of the

amplifier.

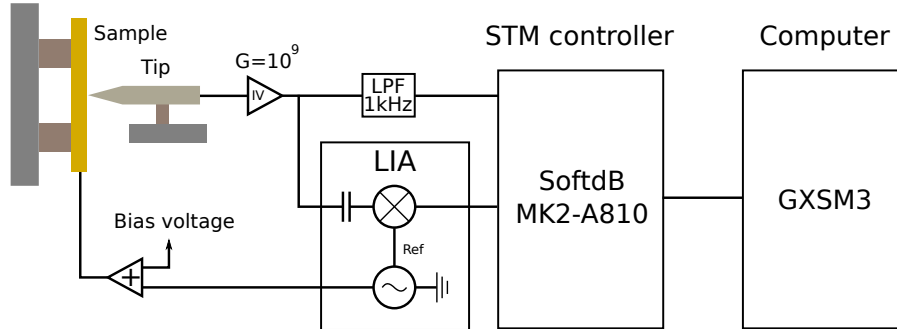


**Figure 5.1:** Adjusted schematic overview of the used STM system to incorporate the changes needed to perform IETS experiments. For simplicity, the circuits needed for controlling the piezos are omitted. Compared to the setup shown in figure 3.1, the lock-in amplifier is added. The local oscillator is added to the bias. The input of the amplifier is AC coupled to the amplified current.



# Chapter 6

## Conclusion

In this report the set up and calibration of a cryogenic scanning tunneling microscope (STM) is discussed. This setup can potentially be used to research graphene edge junctions. The goal was to set up inelastic electron tunneling spectroscopy (IETS) in order to study the edge chemistry of graphene. However, this goal was unfortunately not reached due to difficulties measuring topographic images at 77 K.

These difficulties are most likely caused by condensation of atmospheric gasses still present in the system. Partial successful experiments were performed using a heating resistor in order to clean the sample. For further experiments, we would suggested to use a heater and thermometer in order to control the heating of the sample and to anneal gold samples in the system.

Gold samples were used to calibrate the  $z$  stage of the STM system both at room and cryogenic temperatures. In order to obtain the calibration values, software was written to correct for piezo hysteresis on the fast scanning axis, flatten the data and obtain the step height of gold terraces in two different ways. A method using a histogram of the height of the sample and a method using line cuts of the sample were used. Both methods yield large uncertainties in the obtained calibration values. Therefore, more experiments are needed in order to find a better calibration value for the  $z$  stage.

Furthermore, highly ordered pyrolytic graphite (HOPG) was measured in the system. These samples will become important in order to calibrate the  $xy$  stage.

In order to perform IETS using this set up, it will be needed to implement a system for heating the sample in a controlled way, besides the pressure

in the system needs to be sufficiently low to eliminate as many particles as possible. Feasible methods for this are suggested in the discussion. Hopefully these suggestions will help reaching the goal for performing IETS on twisted graphene edge junctions.

# Bibliography

- [1] Amedeo Bellunato et al. "Dynamic Tunneling Junctions at the Atomic Intersection of Two Twisted Graphene Edges". In: *Nano Letters* 18.4 (2018), pp. 2505–2510. DOI: 10.1021/acs.nanolett.8b00171.
- [2] Amedeo Bellunato et al. "Chemistry at the Edge of Graphene". In: *ChemPhysChem* 17.6 (2016), pp. 785–801. DOI: <https://doi.org/10.1002/cphc.201500926>. eprint: <https://chemistry-europe.onlinelibrary.wiley.com/doi/pdf/10.1002/cphc.201500926>. URL: <https://chemistry-europe.onlinelibrary.wiley.com/doi/abs/10.1002/cphc.201500926>.
- [3] S. K. Khanna and John Lambe. "Inelastic Electron Tunneling Spectroscopy". In: *Science* 220.4604 (1983), pp. 1345–1351. DOI: 10.1126/science.220.4604.1345. eprint: <https://www.science.org/doi/pdf/10.1126/science.220.4604.1345>. URL: <https://www.science.org/doi/abs/10.1126/science.220.4604.1345>.
- [4] Mark A. Reed. "Inelastic electron tunneling spectroscopy". In: *Materials Today* 11.11 (2008), pp. 46–50. ISSN: 1369-7021. DOI: 10.1016/S1369-7021(08)70238-4. URL: <https://www.sciencedirect.com/science/article/pii/S1369702108702384>.
- [5] Harold J.W. Zandvliet and Arie van Houselt. "Scanning Tunneling Spectroscopy". In: *Annual Review of Analytical Chemistry* 2.1 (2009), pp. 37–55. DOI: 10.1146/annurev-anchem-060908-155213.
- [6] J. Tersoff and D. R. Hamann. "Theory of the scanning tunneling microscope". In: *Phys. Rev. B* 31 (2 Jan. 1985), pp. 805–813. DOI: 10.1103/PhysRevB.31.805. URL: <https://link.aps.org/doi/10.1103/PhysRevB.31.805>.
- [7] Juan Carlos Cuevas and Elke Scheer. *Molecular Electronics*. WORLD SCIENTIFIC, 2010. DOI: 10.1142/7434. eprint: <https://www.worldscientific.com/doi/pdf/10.1142/7434>. URL: <https://www.worldscientific.com/doi/abs/10.1142/7434>.

- 
- [8] Ferdinand Evers et al. “Advances and challenges in single-molecule electron transport”. In: *Rev. Mod. Phys.* 92 (3 July 2020). DOI: 10.1103/RevModPhys.92.035001. URL: <https://link.aps.org/doi/10.1103/RevModPhys.92.035001>.
- [9] M. Büttiker et al. “Generalized many-channel conductance formula with application to small rings”. In: *Phys. Rev. B* 31 (10 May 1985), pp. 6207–6215. DOI: 10.1103/PhysRevB.31.6207. URL: <https://link.aps.org/doi/10.1103/PhysRevB.31.6207>.
- [10] J. J. Sakurai and Jim Napolitano. *Modern Quantum Mechanics*. 2nd ed. Cambridge University Press, 2017. DOI: 10.1017/9781108499996.
- [11] Jose Manuel Blanco, Fernando Flores, and Rubén Pérez. “STM-theory: Image potential, chemistry and surface relaxation”. In: *Progress in Surface Science* 81.10 (2006), pp. 403–443. ISSN: 0079-6816. DOI: 10.1016/j.progsurf.2006.07.004. URL: <https://www.sciencedirect.com/science/article/pii/S0079681606000542>.
- [12] D.J. Griffiths. *Introduction to Quantum Mechanics*. Cambridge University Press, 2017. ISBN: 9781107179868.
- [13] John G. Simmons. “Generalized Formula for the Electric Tunnel Effect between Similar Electrodes Separated by a Thin Insulating Film”. In: *Journal of Applied Physics* 34.6 (1963), pp. 1793–1803. DOI: 10.1063/1.1702682.
- [14] John G. Simmons. “Electric Tunnel Effect between Dissimilar Electrodes Separated by a Thin Insulating Film”. In: *Journal of Applied Physics* 34.9 (1963), pp. 2581–2590. DOI: 10.1063/1.1729774.
- [15] Sifan You et al. “Recent advances in inelastic electron tunneling spectroscopy”. In: *Advances in Physics: X* 2.3 (2017), pp. 907–936. DOI: 10.1080/23746149.2017.1372215.
- [16] C. Julian Chen. *Introduction to Scanning Tunneling Microscopy*. eng. 3rd ed. Monographs on the Physics and Chemistry of Materials. Oxford: Oxford University Press, 2021, p. 496. ISBN: 9780198856559. DOI: 10.1093/oso/9780198856559.001.0001. URL: <https://doi.org/10.1093/oso/9780198856559.001.0001>.
- [17] Femto. *Variable Gain Low Noise Current Amplifier DLPCA-200*. URL: <https://www.femto.de/en/products/current-amplifiers/variable-gain-up-to-500-khz-dlpca.html>.
- [18] SoftdB. *Open Source SPM Controller, Model MK2-A810*. URL: <https://www.softdb.com/scanning-probe-microscopy/mk2-a810/>.
- [19] Percy Zahl et al. “Open source scanning probe microscopy control software package GXSM”. In: *Journal of Vacuum Science & Technology B* 28.3 (2010), C4E39–C4E47. DOI: 10.1116/1.3374719.
- [20] A. I. Oliva et al. “Analysis of scanning tunneling microscopy feedback system”. In: *Review of Scientific Instruments* 66.5 (1995), pp. 3196–3203. DOI: 10.1063/1.1145551.

- [21] PI Ceramic GmbH. *P-111 P-153 Pica Shear actuators*. URL: <https://www.piceramic.com/en/products/piezoceramic-actuators/shear-actuators/p-111-p-151-pica-shear-actuators-102900/#specification>.
- [22] Shuheng Pan. *Piezoelectric motor*. WO1993019494A1. Sept. 1993. URL: [patents.google.com/patent/WO1993019494A1](https://patents.google.com/patent/WO1993019494A1).
- [23] S Mohith et al. "Recent trends in piezoelectric actuators for precision motion and their applications: a review". In: *Smart Materials and Structures* 30.1 (Dec. 2020), p. 013002. DOI: 10.1088/1361-665x/abc6b9. URL: <https://doi.org/10.1088/1361-665x/abc6b9>.
- [24] H Li et al. "Analysis for hysteresis of piezoelectric actuator based on microscopic mechanism". In: *IOP Conference Series: Materials Science and Engineering* 399 (Sept. 2018), p. 012031. DOI: 10.1088/1757-899x/399/1/012031. URL: <https://doi.org/10.1088/1757-899x/399/1/012031>.
- [25] PI Ceramic GmbH. *Displacement Behavior*. URL: <https://www.piceramic.com/en/expertise/piezo-technology/properties-piezo-actuators/displacement-behavior/>.
- [26] Joseph Fu et al. "Correction of Hysteresis in SPM Images by a Moving Window Correlation Method". In: *AIP Conference Proceedings* 1173.1 (2009), pp. 280–284. DOI: 10.1063/1.3251234.
- [27] J. F. Joergensen et al. "Hysteresis correction of scanning tunneling microscope images". In: *Journal of Vacuum Science & Technology B: Microelectronics and Nanometer Structures Processing, Measurement, and Phenomena* 12.3 (1994), pp. 1702–1704. DOI: 10.1116/1.587267.
- [28] Wikipedia. *Bilinear interpolation* — *Wikipedia, The Free Encyclopedia*. <http://en.wikipedia.org/w/index.php?title=Bilinear%20interpolation&oldid=1081914622>. [Online; accessed 24-July-2022]. 2022.
- [29] Massimiliano Cavallini and Fabio Biscarini. "Electrochemically etched nickel tips for spin polarized scanning tunneling microscopy". In: *Review of Scientific Instruments* 71.12 (2000), pp. 4457–4460. DOI: 10.1063/1.1311936.
- [30] I. Oádal and P. Sobotík. "STM study of Au(111) growth on mica". In: *Czechoslovak Journal of Physics* 47.4 (Apr. 1997), pp. 445–449. ISSN: 1572-9486. DOI: 10.1023/A:1021267308425.
- [31] Mark H. Dishner et al. "Preparation of gold thin films by epitaxial growth on mica and the effect of flame annealing". In: *Journal of Vacuum Science & Technology A* 16.6 (1998), pp. 3295–3300. DOI: 10.1116/1.581536.
- [32] J. V. Barth et al. "Scanning tunneling microscopy observations on the reconstructed Au(111) surface: Atomic structure, long-range superstructure, rotational domains, and surface defects". In: *Phys. Rev. B* 42 (15 Nov. 1990), pp. 9307–9318. DOI: 10.1103/PhysRevB.42.9307.

- [33] V. Yu. Yurov and A. N. Klimov. "Scanning tunneling microscope calibration and reconstruction of real image: Drift and slope elimination". In: *Review of Scientific Instruments* 65.5 (1994), pp. 1551–1557. DOI: 10.1063/1.1144890.
- [34] Gábor Mándi, Gilberto Teobaldi, and Krisztián Palotás. "Contrast stability and 'stripe' formation in scanning tunnelling microscopy imaging of highly oriented pyrolytic graphite: the role of STM-tip orientations". In: *Journal of Physics: Condensed Matter* 26.48 (Oct. 2014), p. 485007. DOI: 10.1088/0953-8984/26/48/485007. URL: <https://doi.org/10.1088/0953-8984/26/48/485007>.
- [35] Mark T McDermott and Richard L McCreery. "Scanning tunneling microscopy of ordered graphite and glassy carbon surfaces: electronic control of quinone adsorption". In: *Langmuir* 10.11 (1994), pp. 4307–4314.
- [36] Wei Han et al. "Toward Single-Atomic-Layer Lithography on Highly Oriented Pyrolytic Graphite Surfaces Using AFM-Based Electrochemical Etching". In: *Nanomanufacturing and Metrology* 5.1 (Mar. 2022), pp. 32–38. ISSN: 2520-8128. DOI: 10.1007/s41871-022-00127-9.
- [37] Wen Wang et al. "Modeling and Compensation of Dynamic Hysteresis with Force-Voltage Coupling for Piezoelectric Actuators". In: *Micromachines* 12.11 (2021). ISSN: 2072-666X. DOI: 10.3390/mi12111366. URL: <https://www.mdpi.com/2072-666X/12/11/1366>.
- [38] Nathanael van den Berg. "Twisted Edge Tunneling Junction Towards Cryogenic Conditions". BSc Thesis. the Netherlands: Universiteit Leiden, 2021.
- [39] D. Porath et al. "Annealing study of gold films using scanning tunneling microscopy". In: *Journal of Vacuum Science & Technology A* 13.3 (1995), pp. 1165–1170. DOI: 10.1116/1.579855.
- [40] Paul K. Hansma. "Inelastic electron tunneling". In: *Physics Reports* 30.2 (1977), pp. 145–206. ISSN: 0370-1573. DOI: 10.1016/0370-1573(77)90054-0. URL: <https://www.sciencedirect.com/science/article/pii/0370157377900540>.

# Appendix **A**

## Data for other data sets for Au on Mica at room temperature

These figures are the figures visualizing the rough data used in section 4.1.  
The data from the following figures are shown in figure 4.4.

## A.1 Data 30 May 2022

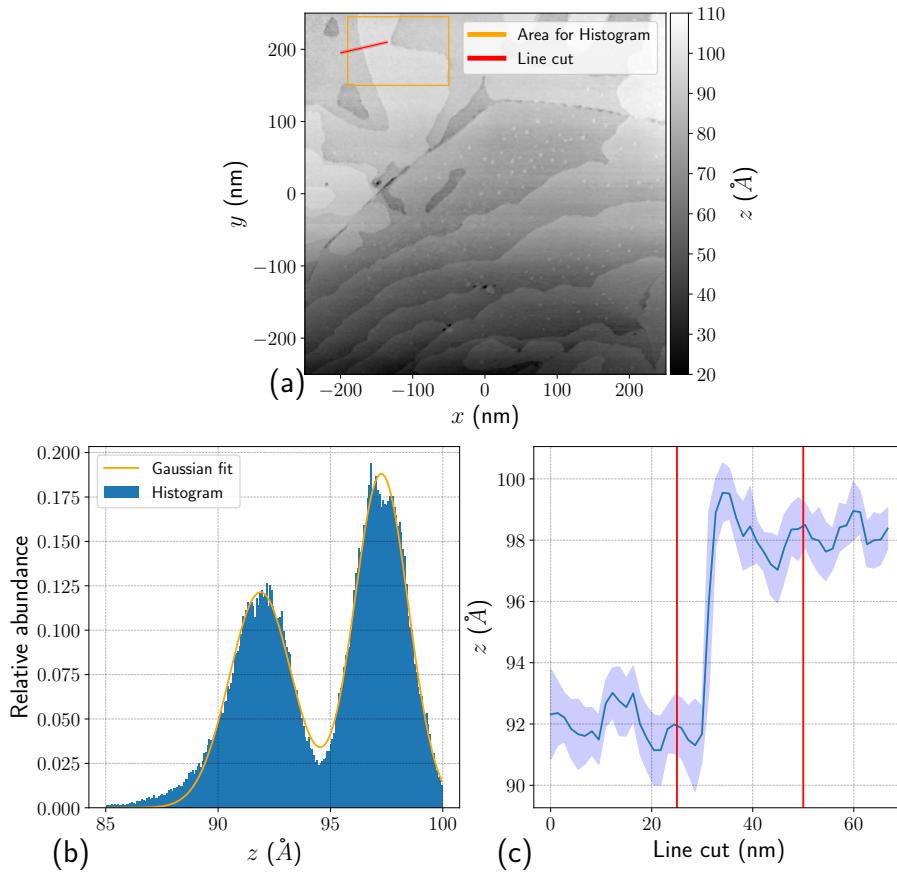


**Figure A.1:** (a) Image of the measurement used for the data analysis. In orange the area used for making the histogram in b is shown. In red the line for the line cut is shown. The width of the red line is the width used for averaging the data for the line cut. (b) Histogram of the orange region shown in the first image. The blue bars give the measured data. The orange line is the fit of two Gaussian functions made to this data. (c) Data of the line cut shown by the red line in the first figure. The blue line is the average height around along the width of the line, the light blue area is the standard error on this value. The red lines indicate the points where the height is determined for finding the terrace height.



## A.2 Data 28 June 2022

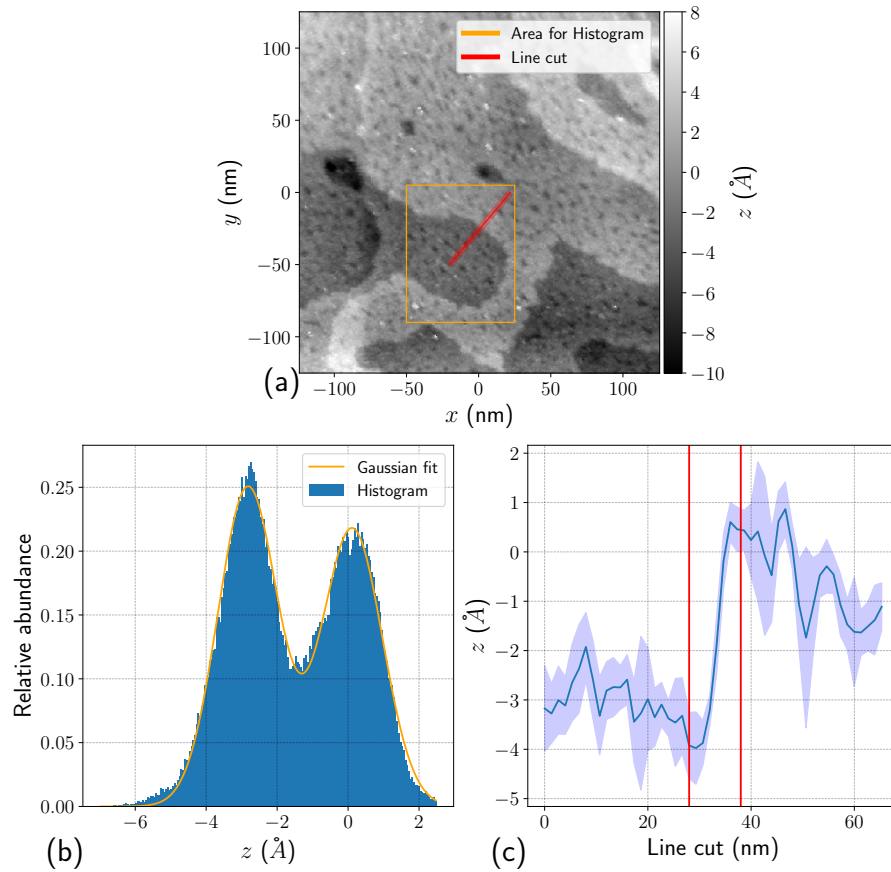


**Figure A.2:** (a) Image of the measurement used for the data analysis. In orange the area used for making the histogram in b is shown. In red the line for the line cut is shown. The width of the red line is the width used for averaging the data for the line cut. (b) Histogram of the orange region shown in the first image. The blue bars give the measured data. The orange line is the fit of two Gaussian functions made to this data. (c) Data of the line cut shown by the red line in the first figure. The blue line is the average height around along the width of the line, the light blue area is the standard error on this value. The red lines indicate the points where the height is determined for finding the terrace height.

## A.3 Data 29 June 2022

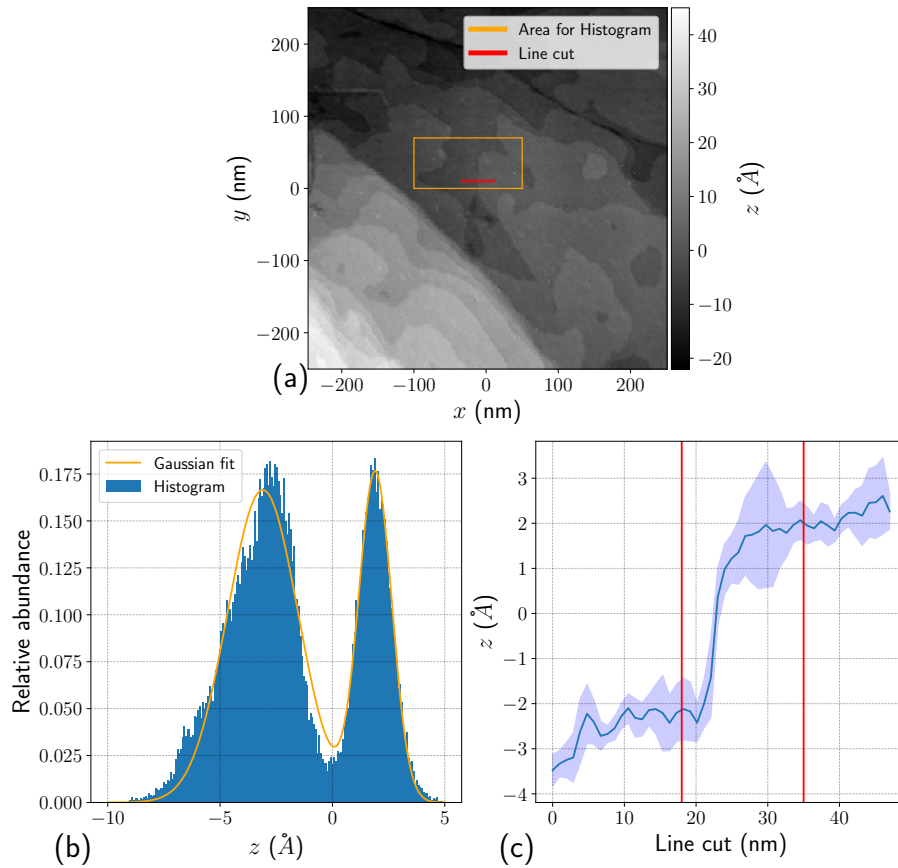


**Figure A.3:** (a) Image of the measurement used for the data analysis. In orange the area used for making the histogram in b is shown. In red the line for the line cut is shown. The width of the red line is the width used for averaging the data for the line cut. (b) Histogram of the orange region shown in the first image. The blue bars give the measured data. The orange line is the fit of two Gaussian functions made to this data. (c) Data of the line cut shown by the red line in the first figure. The blue line is the average height around along the width of the line, the light blue area is the standard error on this value. The red lines indicate the points where the height is determined for finding the terrace height.

## A.4 Data 12 July 2022

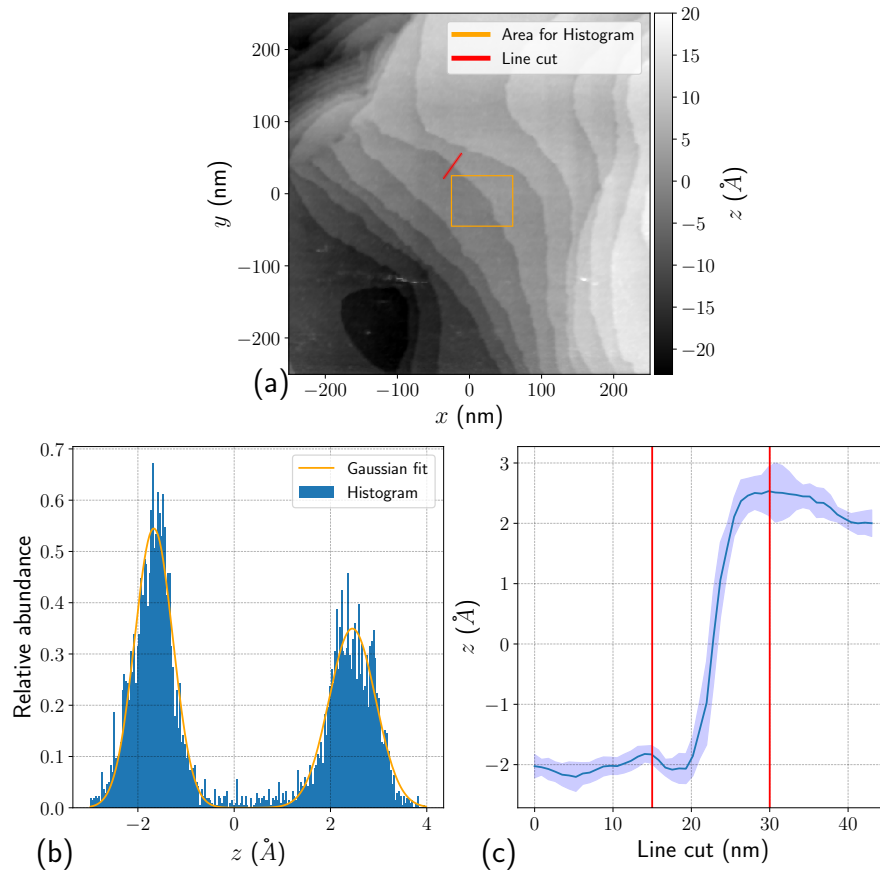


**Figure A.4:** (a) Image of the measurement used for the data analysis. In orange the area used for making the histogram in b is shown. In red the line for the line cut is shown. The width of the red line is the width used for averaging the data for the line cut. (b) Histogram of the orange region shown in the first image. The blue bars give the measured data. The orange line is the fit of two Gaussian functions made to this data. (c) Data of the line cut shown by the red line in the first figure. The blue line is the average height around along the width of the line, the light blue area is the standard error on this value. The red lines indicate the points where the height is determined for finding the terrace height.